Role of precursor microstructure in the development of graphene quantum dots from biomass

Aumber Abbas[a*], Saleem Abbas[b], Tanveer A Tabish[c], Steve J Bull[a], Anh N Phan[a], Tuti Mariana Lim[d*]

[a] School of Engineering, Newcastle University, Newcastle upon Tyne, NE1 7RU, United Kingdom.

[b] School of Materials Science and Engineering, Hebei University of Technology, Tianjin 300130, P. R. China

[c] Department of Bioengineering, Imperial College London, London, SW7 2AZ.

[d] School of Civil and Environmental Engineering, Nanyang Technological University, 639798, Singapore.

[*] Corresponding authors:

School of Engineering, Newcastle University, Newcastle Upon Tyne, NE1 7RU, United Kingdom

Email address: a.abbas2@ncl.ac.uk, dr.aumberabbas@gmail.com (A. Abbas).

School of Civil and Environmental Engineering, Nanyang Technological University, 639798, Singapore.

Email address: TMLim@ntu.edu.sg (T. M. Lim).

Abstract

Renewable, green and cheap biomass could meet the urgent need of cost-effective graphene quantum dots (GQDs) if microstructure and quality can be precisely controlled. Herein, for the first time, we investigate the effect of precursor microstructure on the growth of GQDs from biomass. A novel process is developed which combines carbonisation, oxidation and nitration with controlled hydrothermal fragmentation to form GQDs. The results indicate that aromatic structure of carbon material as a precursor is the key to obtain high-quality GQDs. The as-prepared GQDs possess 3-9 layers graphene structure with an average size of 11.6 ± 1.8 nm and exhibit a moderate quantum yield of 17.5%. These GQDs are used to develop a highly selective and sensitive sensor to detect ferric ions with a detection limit as low as 26 ± 0.4 nM. This study highlights the development of high quality GQDs from biomass for real-world sensing, photocatalytic and biomedical applications.

Keywords

Graphene quantum dots; Microstructure; Biomass; Sustainable synthesis; Sensing

1. Introduction

Graphene quantum dots (GQDs), single or a few layered zero-dimensional derivatives of graphene, have attracted extensive research attention owing to their intriguing size-dependent physicochemical properties and promising applications [1-3]. Owing to the zero dimensionality, quantum confinement and edge effects, GQDs exhibit distinctive electrical and optical properties [4-6]. As an alternate to semiconductor quantum dots (QDs), the GQDs exhibit low cytotoxicity, excellent water solubility, high biocompatibility, tunable bandgap, stable fluorescence and excellent photostability [7-9]. These exceptional properties make GQDs highly attractive in a wide range of science and engineering fields and make them suitable building blocks for numerous applications such as photocatalysis [10-14], photoelectrical conversion [15, 16], bioimaging [17-19], medical diagnostics [8, 20, 21], therapy [19, 22], sensing [18], optoelectronic devices [15, 23] and light-emitting diodes [24, 25]. However, the high cost and quality control remain the key challenges in the preparation of GQDs. Therefore, the development of low cost, pure and high quality GQDs is urgently needed.

A variety of techniques have been employed to develop GQDs using different precursors. These techniques can be classified into commonly employed two main classes: *bottom-up* and *top-down* [2]. The *bottom-up* techniques consist of generating graphene domains from organic molecular precursors through chemical reactions. The *top-down* methods involve the conversion of large graphene domains into smaller ones by chemical cutting. The key limitation in both of these approaches is the use of non-renewable precursors, such as graphene, graphene oxide, carbon fibre, carbon nanotubes, etc. [26-28]. These precursors are rather expensive and

difficult to synthesise. Therefore, the search for renewable, green and inexpensive carbon resource for the cost-effective synthesis of GQDs remains urgently desirable.

To this end, biomass, which is inexpensive, renewable, green and rich in carbon [29-31], stands out as a promising precursor for the cost-effective synthesis of GQDs. A number of reports have been presented on the use of biomass for the cost-effective synthesis of carbon-based QDs [2, 32-36]. However, quality control remains a key challenge which requires urgent attention. Unfortunately, less attention has been paid to investigate the influence of precursor microstructure and properties on the product type and quality. Different plants have different microstructure and composition due to different habitats and varieties. These differences may influence the composition of their derivative carbon materials. As a result, there has been conflicting opinions on the type and quality of product obtained from biomass. A number of researchers adopted the term carbon quantum dots (CQDs) [36-39] for describing their biomass derived product, others suggested these to be GQDs [32, 34, 35], while a few named them polymer quantum dots (PQDs) [40, 41]. For example, Roy et al. studied the transformation of neem leaves extract by hydrothermal treatment into quantum materials, which they called GQDs [34]. On the other hand, Pradeep et al. reported the use of same neem leaves to extract a precursor by a similar hydrothermal treatment and named the product CQDs [38]. In contrast to both studies, Liu et al. reported the hydrothermal treatment of plant (taxus) leaves to synthesise deep red emissive nanoparticles and called these as PQDs [40]. These reports indicate a gap in the true understanding of the product type and role of precursor microstructure in the development of QDs. In fact, the major mechanism involved in the production of these QDs is the *top-down* method, which involves the cutting of precursor carbon domains into nanoscale entities [34, 42]. This suggests that the precursor microstructure has a direct relation

with the product. Therefore, herein we systematically study the role of precursor microstructure in the development of GQDs from biomass.

The development of fluorescence based selective sensors for metal ions detection is appealing due to their direct connection with environment and biological systems. GQDs have emerged as an innovative kind of fluorescence sensors owing to their strong fluorescence, high solubility and superior surface grafting [19, 33, 42]. The sensing and removal of Fe^{3+} have gained extensive attention among different metal ions due to the crucial role of iron in human life and environmental systems [43, 44]. The accumulation of iron was discovered in the neurons of Parkinson's disease patients, therefore, the regulation of Fe^{3+} concentration is critical in controlling the Parkinson's disease [45]. Moreover, Fe^{3+} is among the significant pollutants present in water, triggering the environmental pollution [46]. Therefore, iron content must be precisely measured, recorded and monitored in environmental and biological systems [47]. To accomplish these goals, many scientists have utilised the photoluminescence quenching phenomenon of GQDs by Fe^{3+} [43, 48]. The simple and sensitive detection by a fluorescence-based approach makes GQDs a powerful tool for monitoring harmful metal ions in the environment.

In this study, we present the growth of GQDs from spent tea derived carbon precursors and study the influence of precursor microstructure on the product microstructure and properties. A synthetic approach, which combines the merits of both *bottom-up* and *top-down* techniques was used. The biomass was initially pyrolysed to produce a range of carbonaceous materials with varying microstructures in a *bottom-up* method. These materials were then activated by chemical treatment and hydrothermally cut into nano-fragments in a *top-down* approach (Fig. 1).

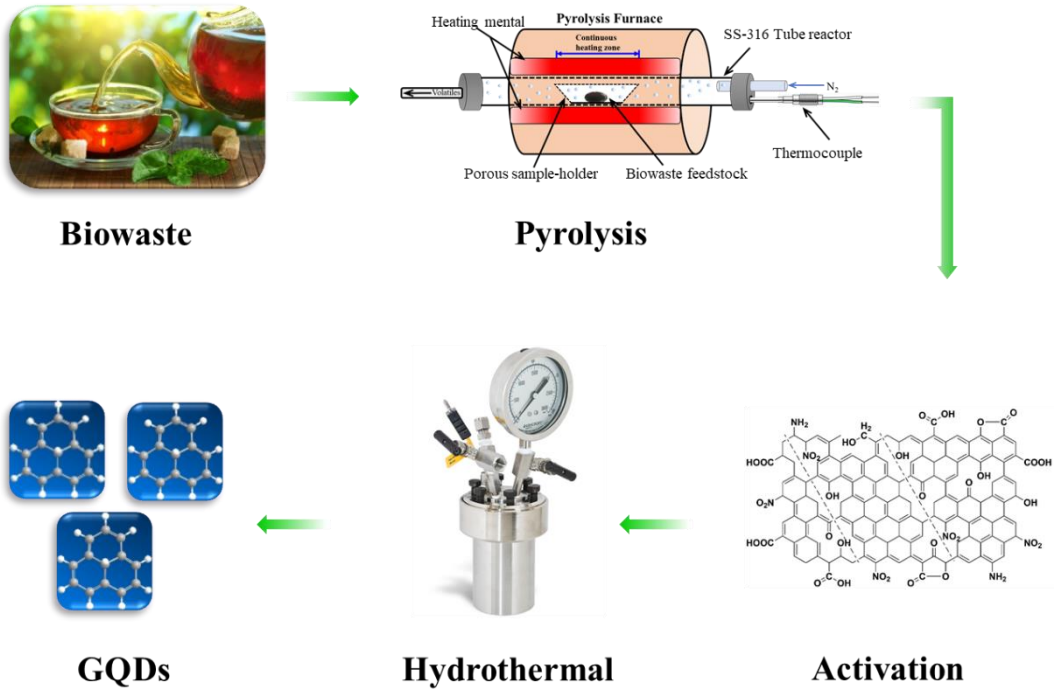

Fig. 1. The schematic representation of the synthesis process for graphene quantum dots (GQDs). A carbon rich precursor is obtained by pyrolysis of biowaste, which is then activated by strong acids followed by hydrothermal treatment to produce GQDs.

A precise control over precursor microstructure leads to GQDs with promising optical properties for potential applications, such as sensing. As a proof of concept, these GQDs were utilised as a fluorescence probe for the detection of metal ions in aqueous media. A GQDs based sensor was designed to selectively detect ferric ions (Fe^{3+}) with high sensitivity. The present study develops the fundamental understanding of the role of precursor microstructure in the growth of GQDs with enhanced optical properties.

2. Materials and methods

2.1. Materials

Spent black tea was derived from PG tips tea bags manufactured by Unilever UK. Sodium hydroxide (NaOH), nitric acid (HNO_3, > 67%) and sulfuric acid (H_2SO_4, > 97%) were purchased from Fisher Scientific, UK. The metal salts $CoCl_2$, $CaCl_2$, $AlCl_3$, $AgNO_3$, $CrCl_3$, $FeCl_2$, $CuCl_2$, $ZnCl_2$, $SrCl_2$, $FeCl_3$, $PbCl_2$, $NiCl_2$, $MoCl_2$, LiCl, NaCl, $MnCl_2$, and $MgCl_2$ were ordered from Sigma Aldrich. Nitrogen gas (99.998% purity) was provided by BOC, UK. The Polyvinylidene fluoride (PVDF) filtration membranes (0.1 μm) were supplied by Merck Millipore, UK. The purification of GQDs was performed using dialysis bags of 1kD MWCO provided by Spectrum Labs, Netherlands. Transmission electron microscopy (TEM) grids \ Mica discs (product code: AGF7013) were obtained from Agar scientific, UK. De-ionised (DI) water was used in all the experiments.

2.2. Synthesis of carbon precursor

Spent tea bags were obtained from a tea shop in Newcastle Upon Tyne, UK. The spent tea was washed thoroughly with DI water to remove the dissolvable organic components (such as colour) and sun dried for a day followed by oven drying at 80 °C overnight (12 hours) for the removal of adsorbed moisture. The dried tea was then ground to fine powder (≤ 90 μm) and stored for further use. The composition of the tea was studied *via* proximate analysis (ASTM standard D3172) and ultimate analysis (ASTM standard D3176) (Table S1, Supplementary Information).

131 The precursor carbon materials were prepared by pyrolysis of spent tea in a horizontal tube
132 furnace (VCTF4, Vecstar Ltd. UK) (Fig. S1, Supplementary Information). The powder samples
133 were loaded onto the furnace and heated to a desired temperature (200-500 °C) at a heating rate
134 of 10 °C min^{-1} in a 50 mL min^{-1} flow rate of nitrogen, followed by a holding time of 3 hours.
135 As a result of variable pyrolysis temperature, carbon materials with varying microstructures
136 were produced. The carbon samples prepared were designated as C-X, where C stands for
137 carbon and X indicates the pyrolysis temperature, e.g. C-500 corresponds to the carbon material
138 prepared at 500 °C.

139

140 ## 2.3. Synthesis of GQDs

141 As-prepared carbon materials were activated with strong acids to incorporate functional groups
142 on the edges and basal planes of the carbon skeleton for efficient cutting into nanosized
143 particles. A 100 mg sample of carbon precursor was mixed in a 100 mL mixture of HNO_3 and
144 H_2SO_4 at a volumetric ratio of 3:1 and sonicated (50-60Hz, 750W) for 15 hours to ensure
145 significant mixing and activation. The acquired dark brown solution was diluted 3 times with
146 DI water and filtered using a 0.1 µm PVDF filtration membrane. The excess acids were
147 removed by washing with large volumes of hot water. The complete removal of excess acids
148 was verified by monitoring the pH of the filtrate.

149 For the synthesis of GQDs, various activated carbon materials were subjected to hydrothermal
150 treatment in a Teflon-lined autoclave (PARR, 4760). In a typical procedure, about 100 mg of
151 the activated carbon was dispersed in 100 mL of water and added to a 300 mL hydrothermal
152 reactor. The reactor was heated and maintained at 200 °C for 12 hours to ensure the significant
153 fragmentation of carbon domains into nanosized pieces. The reactor was then naturally cooled

down to room temperature. The resulting brown suspension was filtered through a 0.1 μm PVDF filtration membrane and dialysed in a dialysis bag for 1 day to remove any impurities. The products acquired from different carbon precursors were designated as C-X-GQDs and are summarised in Table 1.

Table 1. Products obtained from various carbon precursors under identical hydrothermal conditions.

Precursor	Hydrothermal temperature (°C)	Process duration (h)	Product nomination
C-200	200	12	Nanoparticles
C-300	200	12	Nanosheets
C-400	200	12	C-400-GQDs
C-500	200	12	C-500-GQDs

2.4. Sensing of Fe^{+3}

The photoluminescence quenching phenomenon of GQDs by Fe^{3+} was employed to design the sensor. The amount of photoluminescence quenching is associated with the Fe^{3+} concentration. The detection of Fe^{3+} was carried out at 340 nm of excitation in a quartz cuvette. In order to evaluate the selectivity of GQDs towards Fe^{3+} sensing, following 17 different metal ions were selected: Co^{2+}, Ca^{2+}, Ag^{1+}, Al^{3+}, Cr^{3+}, Fe^{2+}, Cu^{2+}, Zn^{2+}, Fe^{3+}, Sr^{2+}, Pb^{2+}, Ni^{2+}, Mo^{2+}, Li^{1+}, Na^{1+}, Mn^{2+} and Mg^{2+}. The concentration of C-500-GQDs was kept constant at 10 μg mL^{-1} and 50 μM of each metal ion was added. The fluorescence spectra were recorded after incubation for 2 minutes. Quantitative measurement of Fe^{3+} was carried out by preparing a series of Fe^{3+} and C-500-GQDs solutions, in which the concentration of GQDs was kept constant but the concentration of Fe^{3+} changed from 0 to 50 μM. The photoluminescence intensities of these solutions were measured using a fluorescence spectrophotometer.

2.5. Characterisation

The properties and structure of the samples were studied at different stages of preparation using various characterisation techniques. The morphological features of the samples were studied by high efficiency scanning electron microscopy (Philips XL30, ESEM-FEG). The microstructure and size of the GQDs were examined by transmission electron microscopy (FEI Titan3™ Themis 300: X-FEG S/TEM) operating at 300 kV. The diameter and size distribution of GQDs were determined from TEM images using the 'ImageJ software (1.46r)'. The number of graphene layers of GQDs was measured using atomic force microscope (AFM) (Park XE-15 AFM) operating in tapping mode. Surface functionalisation and elemental composition were analysed by X-ray photoelectron spectroscopy (XPS) on a Thermo Fisher Scientific NEXSA spectrometer. The surface functional groups were identified using a Bio-Rad Fourier transform infrared spectrometer (FTIR, Cary 630, Agilent Technologies). The crystallinity of samples was examined by Raman spectroscopy using a Renishaw plus Raman spectrometer with 532 nm laser excitation. The fluorescence and ultraviolet-visible (UV-Vis) absorption spectra were recorded using a Shimadzu RF-6000 spectrofluorophotometer and a Shimadzu UV-1800 spectrophotometer, respectively. The spectra were measured with a resolution of 1 nm^{-1}.

3. Results and discussion

3.1. Morphology characterisation

Morphological features of the biomass feedstock and carbon samples were studied by SEM analysis (Fig. 2). A smooth morphology with a few pores is observed for the biomass feedstock (Fig. $2a_1$).

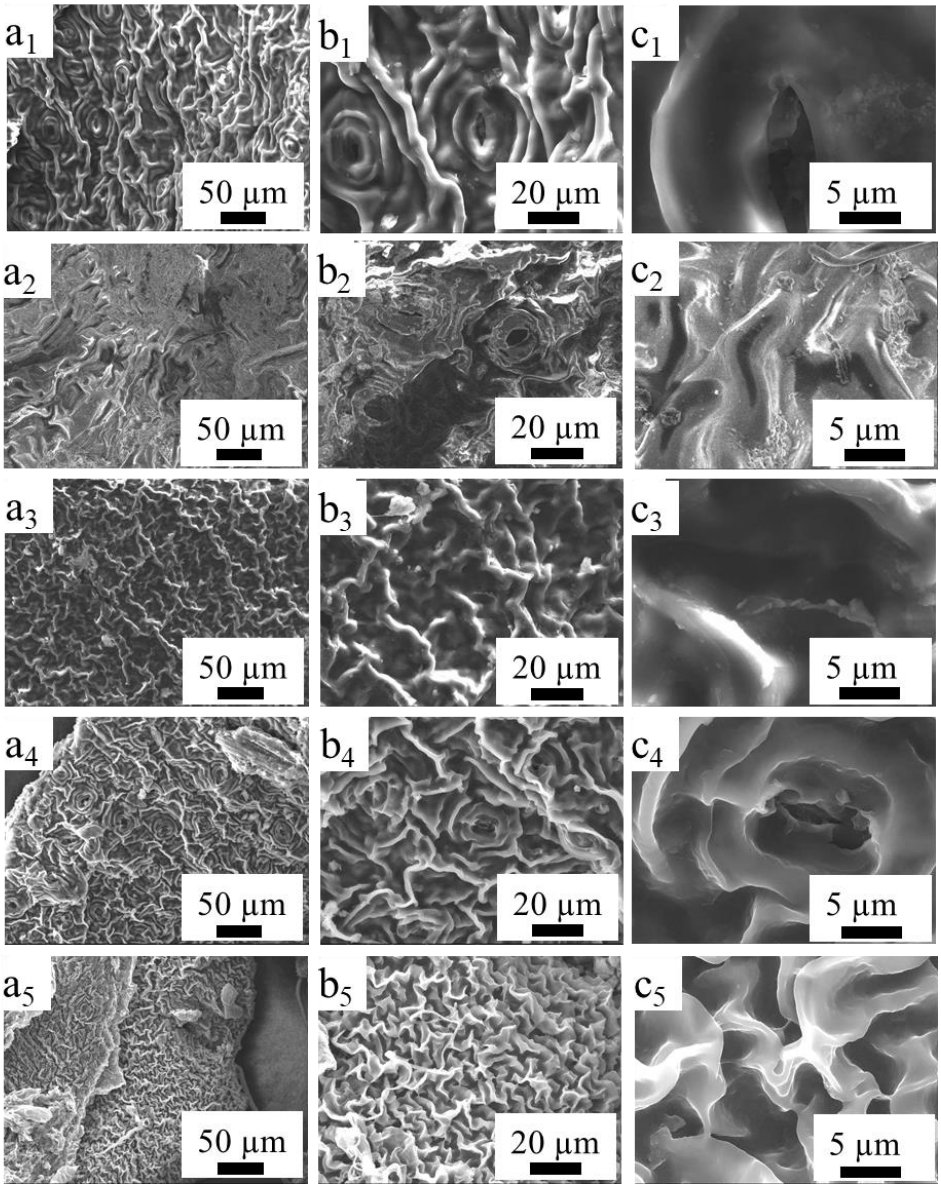

195

196 Fig. 2. Scanning electron microscopy (SEM) images of raw biomass (a_1, b_1, c_1) and its carbon material derivatives
197 obtained via pyrolysis treatment at 200 °C (a_2, b_2, c_2), 300 °C (a_3, b_3, c_3), 400 °C (a_4, b_4, c_4) and 500 °C (a_5, b_5, c_5).

198

199 The higher magnification images further verify the structure and show micrometre sized pores
200 at the centre of a flower-like morphology (Fig. 2b_1, c_1). The morphology of the biomass
201 changes significantly with the pyrolysis treatment. The SEM images of carbon materials

synthesised at 200 °C show a very heterogeneous morphology and irregular structure due to dehydration and the beginning of decarboxylation reactions (Fig. $2a_2$-c_2) [49].

It has been reported [50] that the decomposition of hemicellulose is dominant at a temperature range of ≥ 200-230 °C, cellulose decomposition dominates at 260-290 °C and the lignin decomposition takes place along with cellulose above 290 °C and continues up to 600 °C. As the temperature is increased the volatile compounds start to be removed, consequently the morphology of biomass derivatives begins developing to a more ordered configuration. At 400 °C an improved surface morphology is observed (Fig. $2a_4$-c_4). With further increase in temperature to 500 °C (Fig. $2a_5$-c_5), the morphology of the carbon material develops into a well-ordered structure, resulting in a layered graphene like configuration [51, 52]. These findings indicate that increasing the pyrolysis temperature up to 500 °C provides a carbonised material with well-defined graphene like morphology.

3.2. Structural analysis of carbon materials

The surface and structural characteristics of the carbon samples were investigated using Raman and FTIR spectroscopies. The FTIR spectra of the biomass feedstock and its derivative carbon materials are shown in Fig. 3a. The spectra display a wide band at ~3350 cm^{-1} related to the stretching vibrations of N-H and O-H groups, whereas the bands at around 2900 and 2850 cm^{-1} are attributed to aliphatic C-H (alkane) groups. The bands at about 1735 and 1625 cm^{-1} are assigned to C=O bonds of carbonyl group and C=C bonds in aromatics, respectively. The bands at ~1400-1450 cm^{-1} correspond to the C-C aromatic groups. The multiple bands at 1200-1300 cm^{-1} correspond to the presence of O-H group in esters, ethers, carboxylic acids and alcohols.

A sharp band at about 1015 cm^{-1} is related to C-O stretching in the ether groups. The bands at 700-900 cm^{-1} correspond to the aromatic C-H out of plane bending vibrations [53].

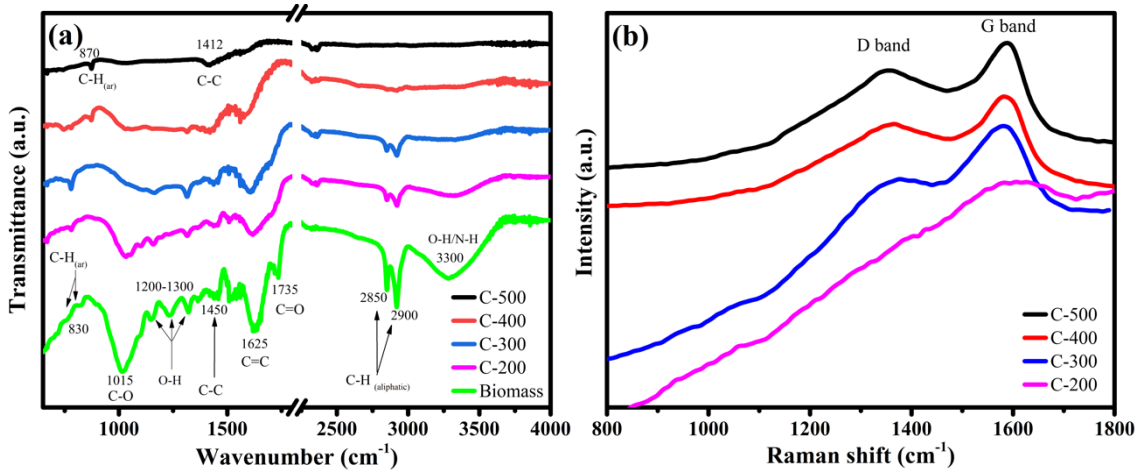

Fig. 3. (a) FTIR spectra of biomass and its derivative carbon samples obtained at different pyrolysis temperatures from 200 to 500 °C. (b) Raman spectra of carbon samples acquired at a range of 200-500 °C.

A continuous reduction in the intensity of these infrared bands is observed with an increase in the pyrolysis temperature. These variations indicate that the major chemical and/or structural changes that take place are attributed to the degradation of cellulose and hemicellulose constituents of the biomass. This process initiates at around 250-300 °C with a maximum decomposition rate at about 370 °C [49] and takes place *via* the breakage of C-H, C-O and C-C bonds by dehydration, decarboxylation and decarbonisation [54]. Whereas, the decomposition of lignin occurs over a wide range (280-600 °C) with a highest degradation rate at about 450 °C [55, 56] to produce phenolic groups [57]. The FTIR peaks due to aliphatic groups at ~2900 cm^{-1} disappear when the pyrolysis temperature rise is > 400 °C. This indicates the removal of aliphatic chains and development of aromatic structure with increase in

241 temperature. This is further confirmed in the 500 °C sample, where peaks related to only
242 aromatic groups at ~1412 (C-C) and ~870 cm^{-1} (C-H) are detectable. These findings indicate
243 the growth of aromatic carbon domains at high temperature.

244 In order to gain further insight into the structure of the biomass derived carbon materials Raman
245 analysis was performed. Raman spectra of carbon materials acquired from the pyrolysis of
246 biomass at 200-500 °C are presented in Fig. 3b. The Raman spectra consist of two distinct
247 bands at ~1360 and ~1587 cm^{-1} designated as the D and G bands respectively, which are
248 indicative of a carbonaceous structure. The D band is related to the defects and disorder in
249 carbon lattice, while G band is attributed to graphitic order or the vibration of sp^2 bonded
250 carbon atoms in a 2D hexagonal lattice of a carbon material [58]. It can be seen in Fig. 3b that
251 C-200 and C-300 exhibit non-uniform Raman spectra and D and G bands are not very clear.
252 This indicates incomplete carbonisation of the biomass at such a low temperature. On the other
253 hand, C-400 and -500 display obvious D and G bands and the intensity of G band increases
254 with the pyrolysis temperature, suggesting the development of graphitic order in the carbon
255 materials. The intensity ratio 'I_D/I_G' indicates the degree of crystallinity and sp^2 content of a
256 carbon material [59]. Our results show I_D/I_G ratio of about 0.85 and 0.80 for C-400 and C-500
257 carbon samples, respectively, which clearly demonstrates their increasing crystallinity and sp^2
258 content with pyrolysis temperature and a dominant value for C-500 sample [59].

259 The elemental composition of the carbon materials prepared at different pyrolysis temperatures
260 was studied by CHN analysis and the results are summarised in Table 2. The carbon content
261 increases and hydrogen content decreases with an increase in the pyrolysis temperature, which
262 is consistent with a carbonisation process. The carbon content is significantly increased in the
263 case of C-500 carbon material which further verifies the removal of volatiles and formation of
264 a graphitic structure.

Table 2. Elemental analysis (dry and ash free basis) of carbon materials prepared at different temperatures.

Sample	Pyrolysis temperature	Carbon	Hydrogen	Nitrogen	Oxygen*
Black tea	Dried at 80 °C	44.82	5.69	3.98	45.51
C-200	200 °C	52.38	4.89	4.63	38.1
C-300	300 °C	64.97	4.54	5.21	25.28
C-400	400 °C	68.26	3.46	5.19	23.09
C-500	500 °C	71.09	2.24	5.18	21.49

*Calculated by difference.

3.3. Activated carbon characterisation

Activation is the process of increasing the tendency of a substance to undergo a chemical reaction. Among the numerous approaches developed, activation of carbon materials with strong acids is a widely accepted approach for their conversion into graphene-based materials. We conducted the activation of carbon materials with individual acids and acid mixtures for investigating their effect on the properties of the product. A mixture of acids was found to be more promising leading to improved optical properties of the product (see Fig. S2, Supplementary Information).

The activation of carbon materials was verified by FTIR spectroscopy. The FTIR spectrum of a representative activated carbon sample shows that activation led to the incorporation of organic functional groups into the carbon structure compared to a non-activated sample (Fig. 4a). The first major difference between the activated and non-activated sample is the appearance of a broad band at ~3000-3500 cm^{-1} after activation, which is attributed to the stretching vibrations of amine (N-H) and hydroxyl (O-H) groups.

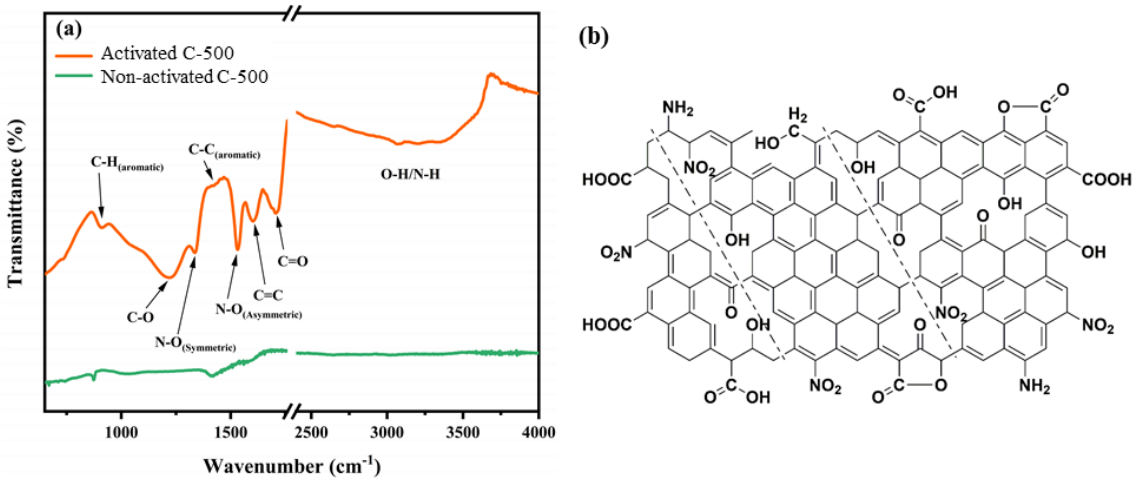

Fig. 4. (a) FTIR analysis of C-500 before (green) and after (orange) activation with a mixture of HNO_3 and H_2SO_4 (3:1 vol.%). (b) Schematic illustration of oxygenated, hydroxyl and nitro groups on the surface and basal planes of sp^2 carbon domains.

Another distinction is the introduction of carbonyl (C=O @~1700 cm^{-1}) and ether (C-O @~1230 cm^{-1}) groups after activation. The last major change is the appearance of bands at ~1530 cm^{-1} and ~1340 cm^{-1} related to asymmetric and symmetric stretching vibrations of nitro (N-O) groups, respectively [60]. These findings indicate the introduction of large number of oxygenated and nitro- functional groups in the carbon matrix after activation, as depicted in the schematic illustration in Fig. 4b. The addition of these functional groups facilitates the fragmentation of carbon domains into nanosized QDs.

The activation of carbon materials was further verified by XPS analysis. Fig. 5 shows the XPS spectra of non-activated and activated carbon samples. Three major peaks are identified at ~285, ~400 and ~532 eV, which are related to C1s, N1s and O1s, respectively. Interestingly the Ca impurity peak (347 eV) observed in the non-activated carbon sample (Fig. 5a) has been completely removed after activation (Fig. 5d).

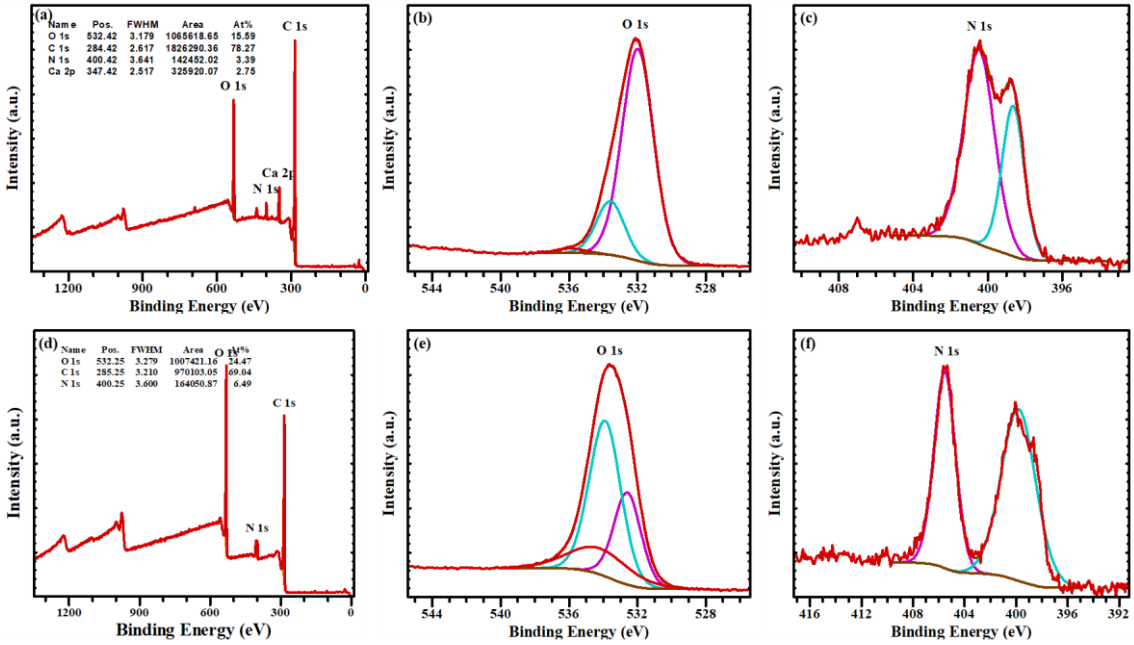

Fig. 5. The XPS survey spectra, high-resolution O1s and N1s spectra of (a, b, c) non-activated and (d, e, f) activated carbon sample C-500, respectively.

A comparison with the non-activated sample indicates that the oxygen and nitrogen contents significantly increased after activation. A relatively high oxygen to carbon ratio (O/C = 35%) was found as compared to non-activated carbon material (O/C = 20%), verifying the extensive oxidation of the carbon materials. Another interesting observation is the presence of a high concentration of N-oxides in activated carbon materials. The band at higher energy (405.5 eV) that appears due to activation (Fig. 5f) is attributed to N-oxides (NO_2^-) [60, 61]. These N-oxides play a vital role in the strong activation of carbon and its fragmentation into GQDs. These results suggest that during the activation process, the hydroxyl, oxygenated and nitro groups (-OH, -COOH, -COO, -NO_2 etc.) are added on the surface and basal planes [26]. This increases carbon reactivity and the hydrophilic character of the material. Consequently, this highly reactive carbon becomes suitable for disintegration into GQDs by hydrothermal treatment.

In contrast with the generally employed acid-base neutralisation, a hot water washing technique was introduced to remove the excess acids. The complete removal of excess acids was verified by monitoring pH. The elimination of the acid-base neutralisation process led to removal of salt generation. Thus, no external impurities were introduced, and highly pure product was obtained. On the other hand, when the same sample was extensively washed with normal water, neutral pH was not attained and neutralisation with a strong base (e.g. NaOH) was an inevitable requirement. This neutralisation process introduces sodium (Na) impurities in the product. (Fig. S3, Supplementary Information). Thus, extensive washing with hot water and elimination of the neutralisation step played a key role in the formation of a highly pure product.

3.4. Characterisation of GQDs

The products obtained from hydrothermal treatment of various activated carbon samples were characterised using TEM and AFM analyses. Fig. 6 shows TEM images of the products synthesised from hydrothermal treatment of C-200 and C-300 precursors. Fig. 6a shows the formation of large sized (~50-150 nm) carbon nanoparticles with irregular shape and a high degree of agglomeration. On the other hand, utilisation of the C-300 precursor resulted in the generation of carbon nanosheets with a size range of ~30-150 nm (Fig. 6b). These results suggest that C-200 and C-300 might be appropriate for the synthesis of carbon dots and nanosheets but are not suitable precursors for the preparation of GQDs. Since the hydrothermal treatment only involves the breakdown of precursor into small entities, the parent microstructure is retained in the product. Therefore, only large sized particles with high degree of agglomeration or nanosheet formation were observed when the precursors (C-200 and C-300) with little or no sp^2 carbon domains. This is verified by the characterisation profile of the

samples in Fig. 3, where a precursor with good sp^2 content is obtained at temperatures above 400 °C. Heat treatment of biomass below 400 °C does result in carbonisation, however, the thermal degradation products do not fragment into sp^2 carbon domains and are, therefore, not suitable precursors for the synthesis of GQDs.

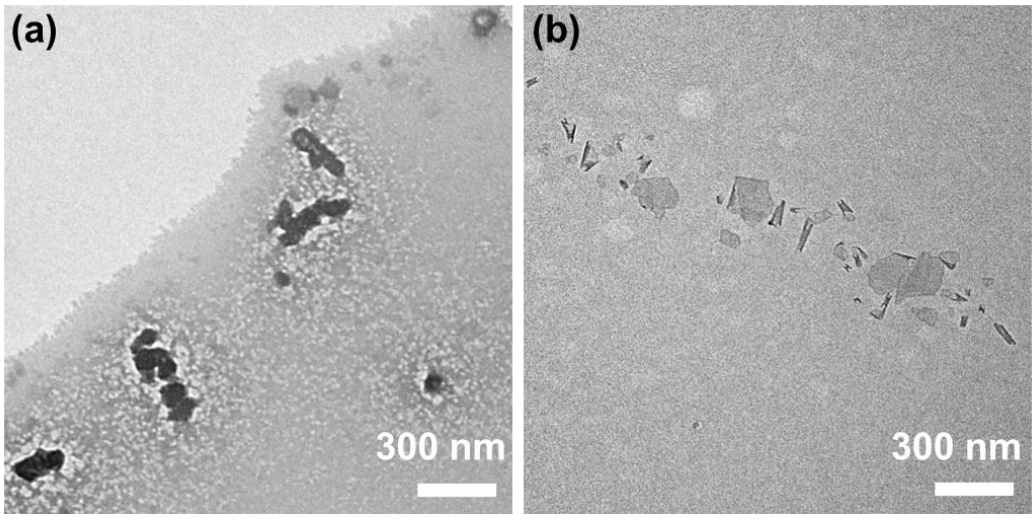

Fig. 6. Transmission electron microscopy (TEM) images of (a) nanoparticles obtained through hydrothermal treatment of C-200 precursor and (b) nanosheets derived from the C-300 precursor.

Fig. 7a shows the TEM image of the product prepared by utilising the C-400 precursor. The formation of GQDs (denoted as C-400-GQDs) with fairly uniform shape and size distribution can be observed. The corresponding histogram in Fig. 7c reveals that as-prepared C-400-GQDs have an average diameter of 30.4 ± 4.4 nm. The nanometre size and dispersion of the GQDs were further confirmed by light scattering. The Tyndall effect (Fig. 7a inset) was noticed in the colloidal suspension of GQDs. Fig. 7b shows a high-resolution TEM (HRTEM) image of C-400-GQDs which indicates their good crystallinity with a lattice spacing of 0.237 nm, related to the $(11\bar{2}0)$ lattice fringes of graphite (0.24 nm) [62].

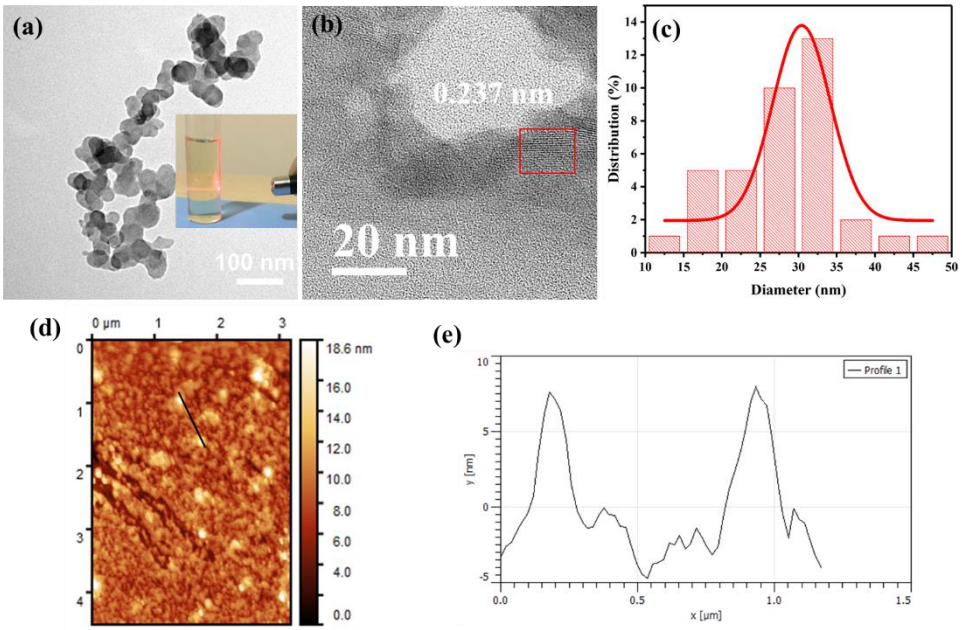

Fig. 7. (a) TEM image (inset is the Tyndall light scattering effect), (b) high-resolution TEM (HRTEM) image, (c) histogram showing the size distribution, (d) atomic force microscopy (AFM) image and (e) AFM height profile of the C-400-GQDs.

As prepared GQDs were further characterised by AFM to gain insight into their thickness. AFM observations (Fig. 7d, e) reveal the typical topographic morphology of GQDs and corresponding height profile, respectively, suggesting that as-prepared GQDs have a thickness of 5-8 nm, corresponding to 15-25 graphene layers. These results indicate the formation of multilayer GQDs. These GQDs also show a small degree of agglomeration.

Finally, sp^2 dominant C-500 precursor was employed for the synthesis of GQDs. The hydrothermal treatment of C-500 precursor resulted in the development of GQDs with a narrow size distribution. Fig. 8a shows the TEM image of evenly dispersed quantum dots (C-500-GQDs) with uniform shape and size distribution. Fine size and even distribution of the C-500-

GQDs without noticeable agglomeration suggest that the C-500 precursor is superior to other precursors utilised for the synthesis of GQDs.

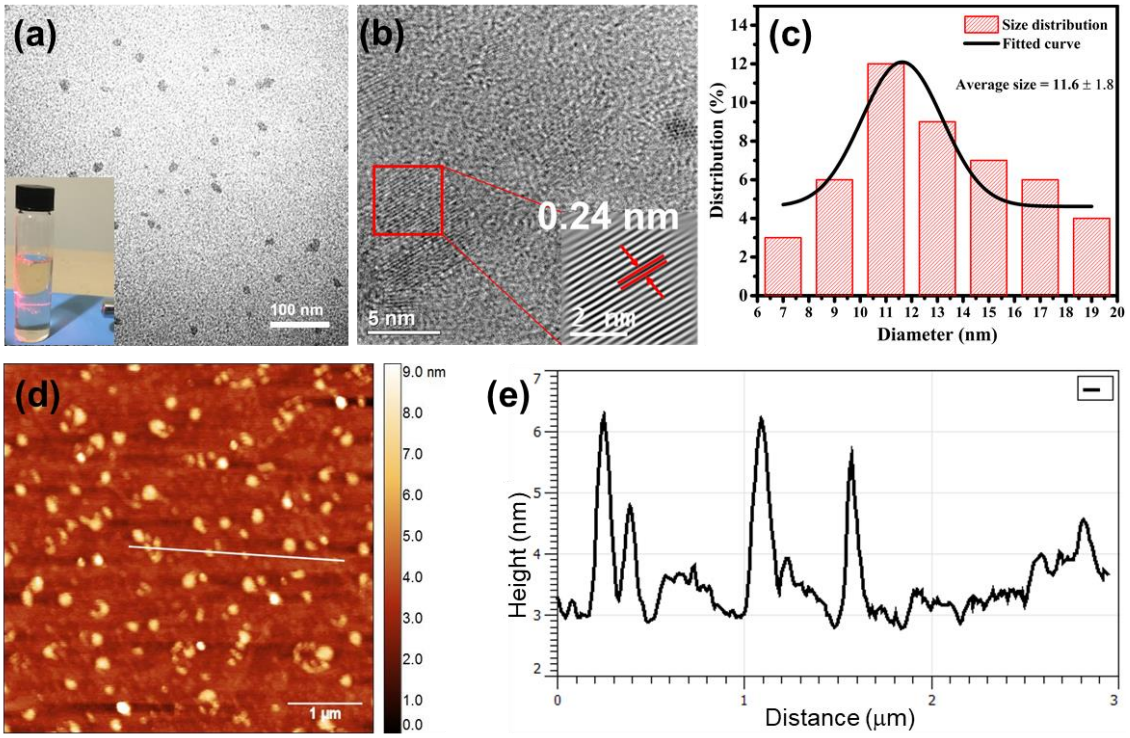

Fig. 8. (a) TEM image, inset is the Tyndall light scattering effect, (b) HRTEM image (inset is the corresponding enhanced image of the square marked in red), (c) histogram showing the size distribution, (d) AFM image and (e) corresponding AFM height profile of the C-500-GQDs.

The size of as-synthesised C-500-GQDs was carefully measured using ImageJ and the results are summarised in Fig. 8c. The C-500-GQDs exhibit a narrow size distribution of 11.6 ± 1.8 nm. The nanometre particle size and dispersion of the GQDs were further verified by light scattering. The Tyndall effect (Fig. 8a inset) was clearly observed in the colloidal suspension of GQDs in water. To confirm the material structure of the product, HRTEM analysis was performed. The HRTEM image (Fig. 8b) shows that C-500-GQDs exhibit excellent

crystallinity and clearly noticeable lattice fringes. Inset is the enhanced image of the region marked by a square and displays a lattice parameter of 0.24 nm corresponding to the $(11\bar{2}0)$ lattice fringes of graphite [62]. In order to get further insight into the thickness, C-500-GQDs were characterised by AFM analysis. The AFM image of C-500-GQDs (Fig. 8d) shows a typical topographic morphology and corresponding height profiles (Fig. 8e, f) indicate a thickness of 1 to 3 nm, corresponding to 3-9 layers of graphene. The AFM analysis of C-400-GQDs and C-500-GQDs reveal a good control over the lateral size of GQDs. The lateral size of C-500-GQDs is smaller than that of C-400-GQDs. The small lateral dimension confirms the graphene nature of these QDs, since the carbon dots have lateral dimension similar to the diameter. These results indicate that the C-500 precursor with dominant sp^2 content and aromatic structure is the best among all precursors tested for the synthesis of high quality GQDs. On the other hand, partially carbonised precursors containing little or no content of sp^2 structure are found not suitable for the synthesis of GQDs. These findings reveal that development of sp^2 carbon domains and aromatic structure of the precursor material is critical to synthesise GQDs.

3.5. Structural studies of GQDs

The surface and structural properties of as-synthesised GQDs were characterised by various spectroscopic techniques. The FTIR spectra of both types of GQDs are presented in Fig. 9a and show a strong absorption of oxygenated functional groups, consistent with the previous reports [63]. Spectra show the presence of hydroxyl/amino groups (O-H/N-H @ 3200-3300 cm^{-1}), carbonyl groups (C=O @ 1685 cm^{-1}), carboxylate groups (O-C=O @ ~1552 cm^{-1}) and plenty of C-O groups at ~1367, ~1230 and ~1097 cm^{-1}. The bands below 1000 cm^{-1} are attributed to

the out of plane bending vibration of aromatic C-H groups [63, 64]. Plenty of oxygenated groups present on the surface of GQDs impart them hydrophilic properties and enhance the luminescence. These functional groups make GQDs soluble in water to make a stable suspension. Interestingly, the absence of NO- groups indicates that large amount of nitro groups present in the activated carbon took part in the fragmentation process and were removed completely from the final product. In addition, the oxygenated functional groups on the surface of GQDs may perform as a passivation layer and hinder their agglomeration [65].

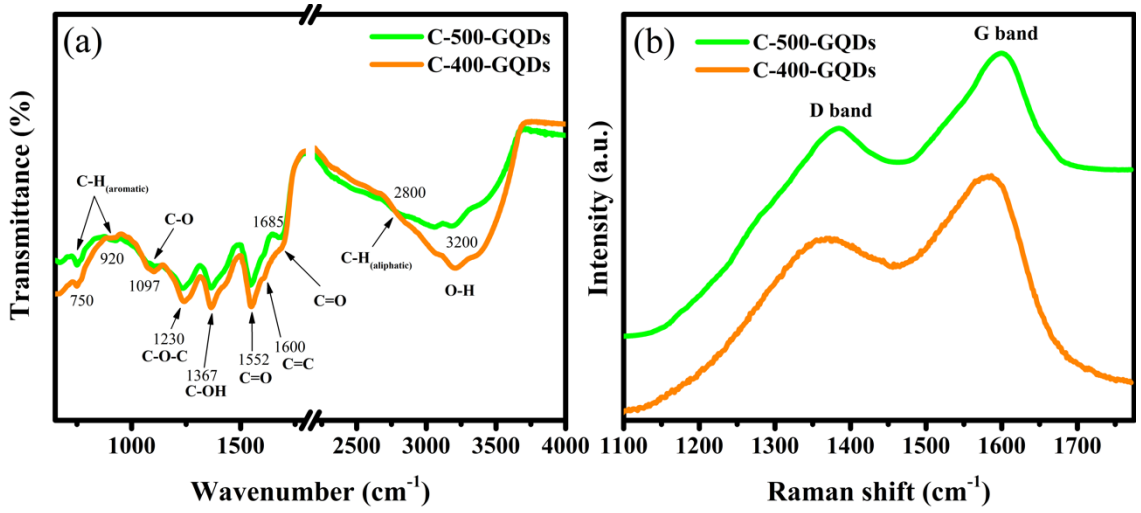

Fig. 9. (a) FTIR spectra of the C-400-GQDs and C-500-GQDs showing different types of functional groups attached on the surface of GQDs. (b) Raman spectra of C-400-GQDs and C-500-GQDs with the bands in the range of 1200-1800 cm^{-1}, typically associated with the graphene materials.

Raman spectra (Fig. 9b) of as-prepared GQDs consist of two distinctive bands: disorder (D) band (1385 cm^{-1}) and crystalline (G) band (1600 cm^{-1}), which are similar to the spectra of their precursor materials. As discussed earlier, the D band is associated with the defects and disorder, while the G band is related to the graphitic order and usually indicates the crystallinity of the

carbon. The G band in graphene is related to E_{2g} phonons at Brillouin zone centre and its frequency decreases with rise in the number of graphene layers [58], therefore, its intensity in C-400-GQDs (15-25 layers) is lower than that of C-500-GQDs (3-9 layers). The I_D/I_G ratios of C-400-GQDs and C-500-GQDs are about 0.89 and 0.88, respectively, which show their good degree of crystallinity and are in good agreement with the previous reports [66, 67]. Interestingly, the I_D/I_G ratios of GQDs are increased as compared to precursors materials, possibly due to the edge states at the periphery of GQDs [67].

To confirm the products obtained in this study are indeed GQDs and not their carbon dot counterpart, we performed additional characterisation by various techniques such as XPS, XRD, AFM, etc. The XRD pattern of the purified product exhibit one prominent peak at 2θ value of 24-25° corresponding to (002) plane of graphite (Fig. S4, Supplementary Information). This specifies the existence of a layered structure, indicating a few layered graphene structure of GQDs. The reason behind broad nature of the XRD band is the small size of GQDs. This is in agreement with the previous reports [42, 68].

The surface functionalisation and elemental composition of GQDs was examined by XPS analysis. The survey XPS spectrum of the C-500-GQDs shows three peaks corresponding to C1s (284.4 eV), N1s (399.4 eV) and O1s (532.4 eV), respectively (Fig. 10). The XPS analysis shows that the GQDs are primarily composed of C, N and O. The absence of any peaks from impurity atoms (Ca, S, etc.) confirms high purity of the product obtained. The N1s spectrum (Fig. 10c) consists of a single peak at ~399.8 eV, corresponding to the traces of pyridinic/pyrrolic nitrogen present in the product [61]. The XPS shows the absence of N-oxide functionality observed in the activated carbon materials (see Fig. 5f). This further verifies that the N-oxides took part in the cleavage process during the synthesis and were finally removed from the product.

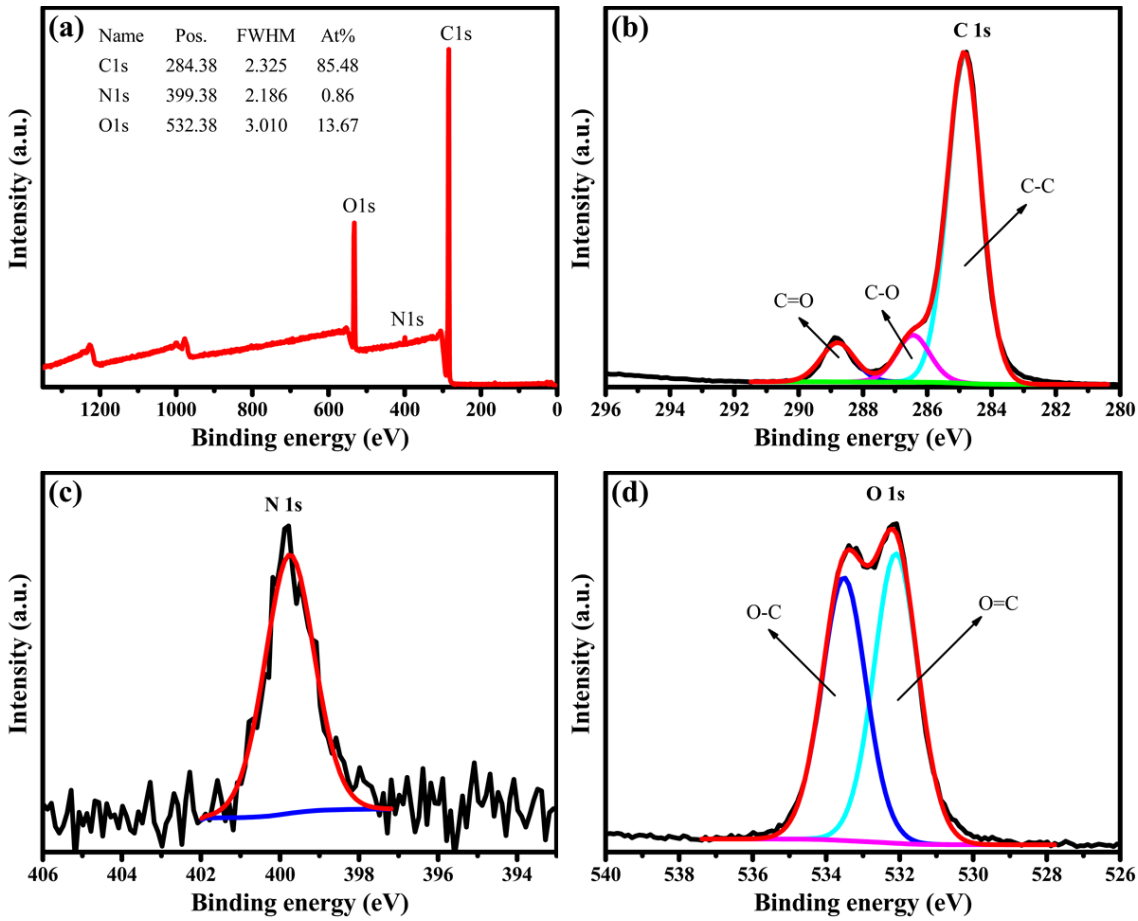

Fig. 10. The (a) XPS survey, (b) C 1s, (c) N 1s, (d) O 1s high-resolution XPS spectra of C-500-GQDs.

The high resolution C1s and O1s spectra indicate the presence of C-O and C=O groups on the surface of GQDs. These results are in good agreement with the results of FTIR which shows the presence of oxygenated groups on the surface of quantum dots. The O/C ratio was found to be ~16%, indicating the oxygenated nature of the GQDs which make them hydrophilic in nature. This is an indication of the development of GQDs, since the carbon dots usually possess high oxygen ratio of over 50% [69, 70]. On the other hand, the O/C ratio of activated carbon materials was ~35%. This supports the idea that oxygenated groups take part in the disintegration process of graphene matrix into GQDs [26]. The controlled introduction of oxygen functionalities in GQDs makes their properties tunable. In addition to XRD and XPS

results, AFM analysis (Fig. 8d) has shown the thickness of C-500-GQDs to be 1-3 nm consisting of 3-9 graphene layers. These results validate that the products obtained are indeed the GQDs and not their carbon dot counterparts.

3.6. Optical properties

The optical properties of as-prepared GQDs were explored by UV-Vis absorbance and photoluminescence spectroscopies. Fig. 11a shows UV-Vis absorption spectrum of C-400-GQDs. A wide absorption band is observed at about 280 to 350 nm with a peak value around 300 nm which is ascribed to the n–π* transition in the carbonyl group, typically noticed in graphene like systems [71]. The 'n' electrons are the unpaired (non-bonding) electrons located on the oxygen of carbonyl group (C=O). Thus, n to π* transition is related to the excitation of one of the unpaired oxygen electrons to the antibonding π* orbital. These findings indicate the UV absorbance in C-400-GQDs is associated with their surface oxygen states (C=O). The bandgap of C-400-GQDs was derived from the absorbance spectrum using a Tauc plot [72] and was determined to be 3.1 eV.

The photoluminescence properties of C-400-GQDs were studied at a wide spectral range from 320 nm to 410 nm excitation (Fig. 11a). At 320-340 nm excitation, no detectable photoluminescence emission was observed which indicates the absence of GQDs with large bandgap. When the C-400-GQDs were excited by a 350 nm laser light, an emission peak at 430 nm was observed. The emission wavelength is larger than the excitation wavelength; this is the well-known Stokes shift. The C-400-GQDs exhibit an increase in photoluminescence intensity with a rise in excitation wavelength and the strongest peak is observed at 465 nm when excited at 390 nm.

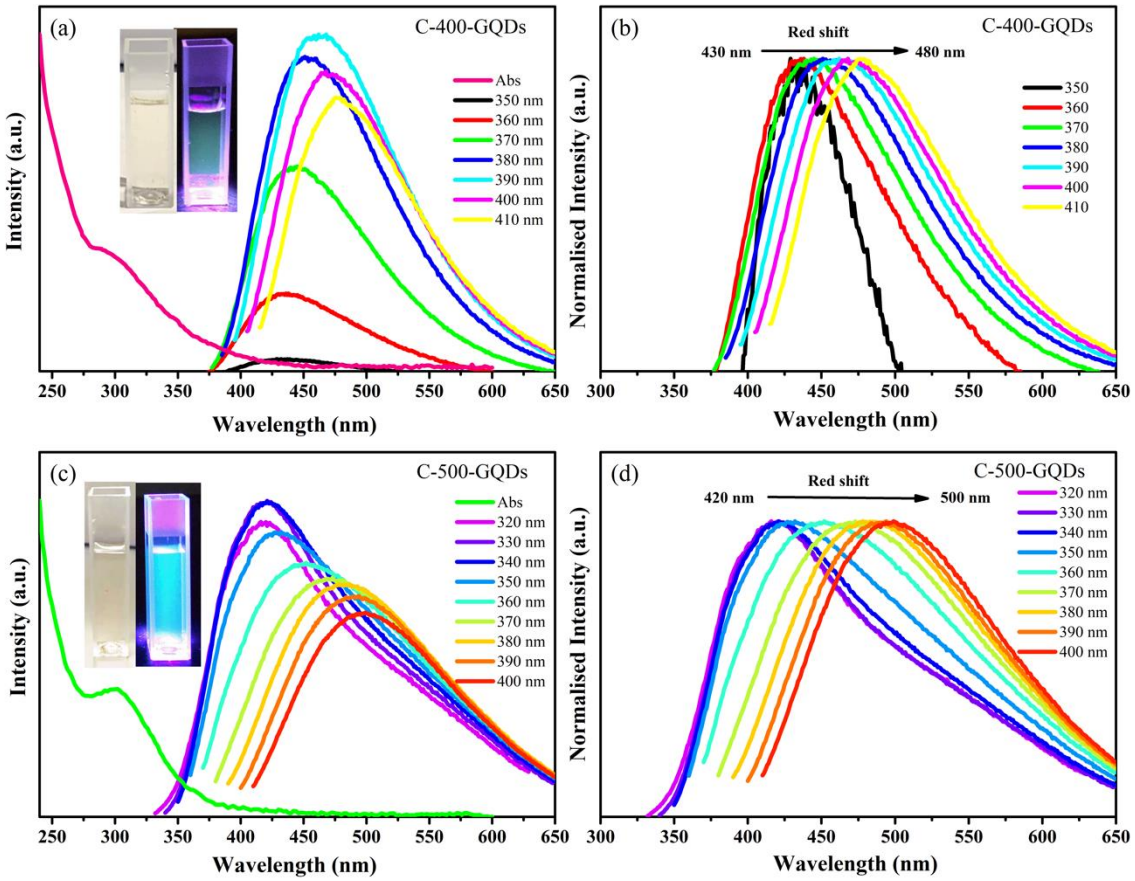

Fig. 11. (a) UV-Vis absorbance and photoluminescence spectra of C-400-GQDs at a range of excitation wavelengths; inset is the GQDs solution under visible and 365 nm UV light, (b) normalised photoluminescence spectra of C-400-GQDs, (c) UV-Vis absorbance and photoluminescence spectra of C-500-GQDs at different excitation wavelengths, inset is the photograph of C-500-GQDs solution under visible and 365 nm UV lamp, and (d) normalised photoluminescence spectra of C-500-GQDs.

The variation in excitation wavelength results in a shift in emission peak position (Fig. 11b). An obvious red-shift of ~50 nm is observed which is attributed to the variable size of C-400-GQDs or the presence of different functional groups [62]. These results indicate that C-400-GQDs exhibit excitation dependent photoluminescence emission as a result of the quantum confinement effect or various emissive states introduced by different functional groups [42, 48]. The inset in Fig. 11a shows the photograph of the C-400-GQDs solution under 365 nm

494 UV and visible light illumination. The GQDs colloidal solution shows a transparent colour in
495 visible light whilst a green fluorescence is seen under UV light.

496 Optical properties of the as-prepared C-500-GQDs were also examined by UV-Vis and
497 photoluminescence spectroscopies. Fig. 11c shows the absorption spectrum of C-500-GQDs.
498 A deep absorption band is noticed in the UV range at about 300 nm. The strong absorption
499 band indicates improved optical properties of C-500-GQDs compared to C-400-GQDs. The
500 band gap of C-500-GQDs based on the absorbance spectrum was calculated to be ~3.3 eV.

501 The fluorescence emission spectra of C-500-GQDs at a range of excitations from 320 to 400
502 nm are presented in Fig. 11d. When excited by a 320 nm laser, these GQDs show emission
503 band at around 415 nm. The most intense emission peak was observed at 420 nm when excited
504 at 340 nm wavelength, which is consistent with previously reported GQDs [33, 35, 42, 62]. It
505 is important to note that the emission peak position shifts towards higher wavelength region
506 with increase in excitation wavelength. As a result, the C-500-GQDs display wide emission
507 spectra from ~420 to ~500 nm. This excitation dependent emission makes these GQDs suitable
508 building blocks for multicolour imaging applications (such as bioimaging). The inset in Fig.
509 11c shows the photograph of C-500-GQDs solution after irradiation by 365 nm UV light and
510 visible light. The GQDs colloidal solution shows a transparent colour under visible light which
511 indicates that these GQDs do not have down-conversion or up-conversion characteristics in
512 visible light. On the other hand, a bright blue fluorescence is revealed under UV light, which
513 shows the excellent photoluminescence properties of C-500-GQDs.

514 The optical properties of C-400-GQDs and C-500-GQDs demonstrate varying characteristics.
515 For further understanding, quantum yields of both types of GQDs were calculated using
516 quinine sulfate as a reference. The quantum yield was estimated by comparing the absorbance

values and integrated photoluminescence intensities of GQDs with that of quinine sulfate (see Supplementary Information for details). The quantum yields of C-400-GQDs and C-500-GQDs were calculated to be 8.2% and 17.5%, respectively. The C-500-GQDs which were derived from a precursor with more sp^2 content and aromatic microstructure, exhibit superior optical properties. These results further validate the role of precursor microstructure in the development and optical properties of GQDs. Moreover, the variable size of these GQDs leads to an adjustable bandgap, which is consistent with previous reports [73, 74]. A decrease in GQDs size leads to a shift in photoluminescence emission at higher energy [70, 75-77]. Thus, based on the TEM results, small sized C-500-GQDs exhibit a blue shift in emission maxima (415 nm) compared to large sized C-400-GQDs (465 nm). This is further confirmed in the inset in Fig. 11a and c, where the solution of GQDs under 365 nm excitation changes colour from light green to strong blue. These results indicate that the bandgap of our GQDs can be tuned by varying their size and thus the photoluminescence properties can be controlled. The tunable photoluminescence properties of our GQDs make them suitable building blocks for a range of applications.

The photoluminescence excitation (PLE) spectra of both type of GQDs are presented in Fig. 12a. The PLE of C-400-GQDs was recorded at the strongest luminescence emission 465 nm and a wide excitation band was noticed at ~330 nm. This PLE band corresponds to the absorption band (280-350nm) of C-400-GQDs. The PLE spectra of C-500-GQDs was measured at 415 nm corresponding to the strongest emission maximum. A sharp PLE band was observed at around 300 nm, which is related to the strong absorption band (300 nm) of C-500-GQDs. Thus, the UV-Vis absorbance, photoluminescence and PLE results of our GQDs are consistent.

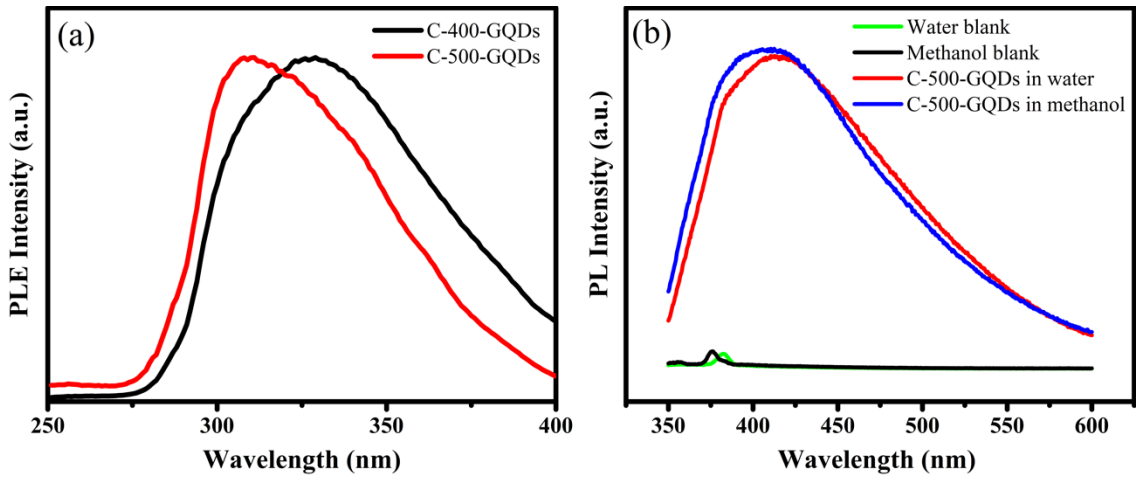

Fig. 12. (a) The normalised photoluminescence excitation (PLE) spectra of C-400-GQDs at 465 nm and C-500-GQDs at 415 nm emission wavelength. (b) Photoluminescence analysis of water (green) and methanol (black) solvents showing no emission; and photoluminescence emission (at 340 nm excitation) of freeze-dried C-500-GQDs dispersed in water (red) and methanol (blue) exhibiting retention of inherent photoluminescence properties with no significant effect of dispersant.

In order to confirm that the photoluminescence properties were not originating from the dispersant or impurities, the photoluminescence properties of the dispersant (water and methanol) were measured as a control sample. As shown in Fig. 12b, the blanks did not show any luminescence with water or methanol only. However, the strong luminesce emission was observed upon the addition of C-500-GQDs in the dispersant. The luminescence properties were almost independent of the dispersant. Moreover, the C-500-GQDs did not lose their luminescence properties after freeze-drying and storing for several months, and the strong emission recovered upon dispersion in a solvent. These results verify strong and stable photoluminescence properties of our as-prepared GQDs, making them suitable for wide range of optoelectronic and sensing applications.

3.7. Application as a sensor

Owing to their strong fluorescence, high solubility and superior surface grafting, GQDs have emerged as an innovative kind of fluorescence sensors [19, 33, 42, 78]. Based on the strong fluorescence properties and extensive presence of oxygenated surface functional groups, the C-500-GQDs are anticipated to be a potential candidate for sensing applications.

In this study, the selective detection of Fe^{3+} was investigated by evaluating the quenching behaviour of C-500-GQDs solution (10 μg mL^{-1}) in the presence of seventeen different metal ions: Co^{2+}, Ca^{2+}, Ag^{1+}, Al^{3+}, Cr^{3+}, Fe^{2+}, Cu^{2+}, Zn^{2+}, Fe^{3+}, Sr^{2+}, Pb^{2+}, Ni^{2+}, Mo^{2+}, Li^{1+}, Na^{1+}, Mn^{2+} and Mg^{2+}. Since C-500-GQDs exhibit a strong photoluminescence emission at 340 nm excitation this excitation wavelength was chosen to study the variation in photoluminescence intensity of GQDs after addition of different metal ions. The photoluminescence emission spectrum of C-500-GQDs was recorded after adding 50 μM of different metal ions with an incubation time of 2 min (Fig. 13a). The emission spectrum showed a slight decline with the addition of Pb^{2+}, Cu^{2+}, or Al^{3+}, however, the emission was substantially quenched upon the addition of Fe^{3+}. Fig. 13 b shows the intensity ratio (F/F_0) of C-500-GQDs in the presence of different metal ions (F and F_0 are the photoluminescence intensities of C-500-GQDs in the presence and absence of different metal ions, respectively). Comparing with the blank (control) sample, the intensity ratio of C-500-GQDs is significantly reduced only by Fe^{3+} among seventeen different metal ions, as demonstrated in Fig. 13b. These findings indicate the strong selective capability of C-500-GQDs for sensing Fe^{3+}.

The photoluminescence quenching mechanism is associated with the strong affinity of Fe^{3+} towards specific surface functional groups, such as hydroxyl/carboxyl groups of C-500-GQDs, resulting in the formation of a stable complex [46]. The fluorescence quenching takes place

when an excited electron partially shifts to the d orbital of Fe^{3+} rather than relaxing radiatively [33, 46]. The affinity of various ions toward C-500-GQDs was investigated in a systematic manner under identical operating conditions. As depicted in Fig. 13c, the affinity of Fe^{3+} toward C-500-GQDs was highest among seventeen unique metal ions. These results suggest the promising potential of C-500-GQDs for selective sensing of Fe^{3+} in aqueous media.

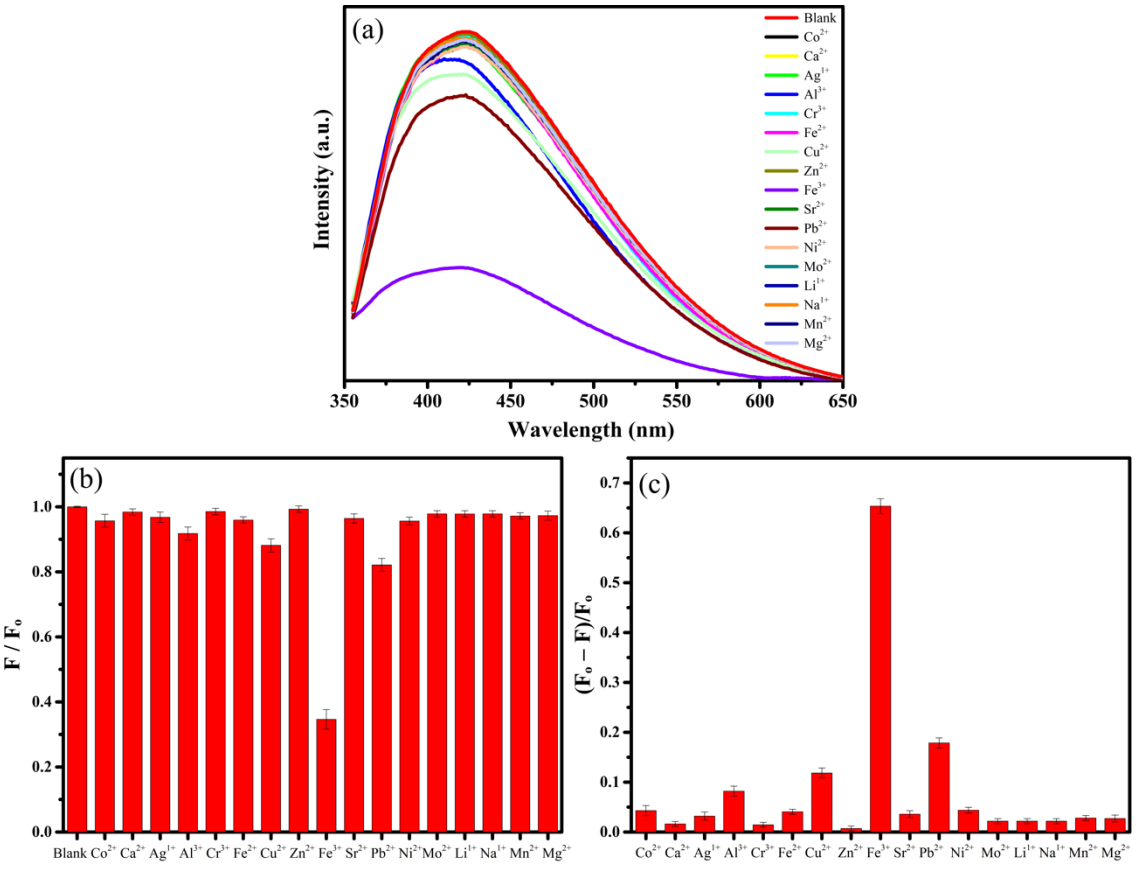

Fig. 13. (a) Photoluminescence emission spectra and (b) intensity ratio (F/Fo) of C-500-GQDs (10 μg mL^{-1}) in the absence (blank) and presence of different metal ions (50 μM) at 340 nm excitation (F and F_0 are the photoluminescence intensities of C-500-GQDs in the presence and absence of different metal ions)). (c) Comparison of the affinity of different metal ions towards C-500-GQDs.

Sensitivity is one of the key factors for real-world sensing applications. The sensitivity of the C-500-GQDs based sensor was investigated by evaluating the influence of various concentrations of Fe^{3+} on photoluminescence intensity of C-500-GQDs. Fig. 14a shows the variation in photoluminescence intensity of C-500-GQDs after the addition of various concentrations of Fe^{3+} (0.1 to 50 μM). The spectra suggest that the photoluminescence intensity of C-500-GQDs is highly sensitive to Fe^{3+} concentration. The photoluminescence quenching intensifies with rise in the concentration of Fe^{3+}.

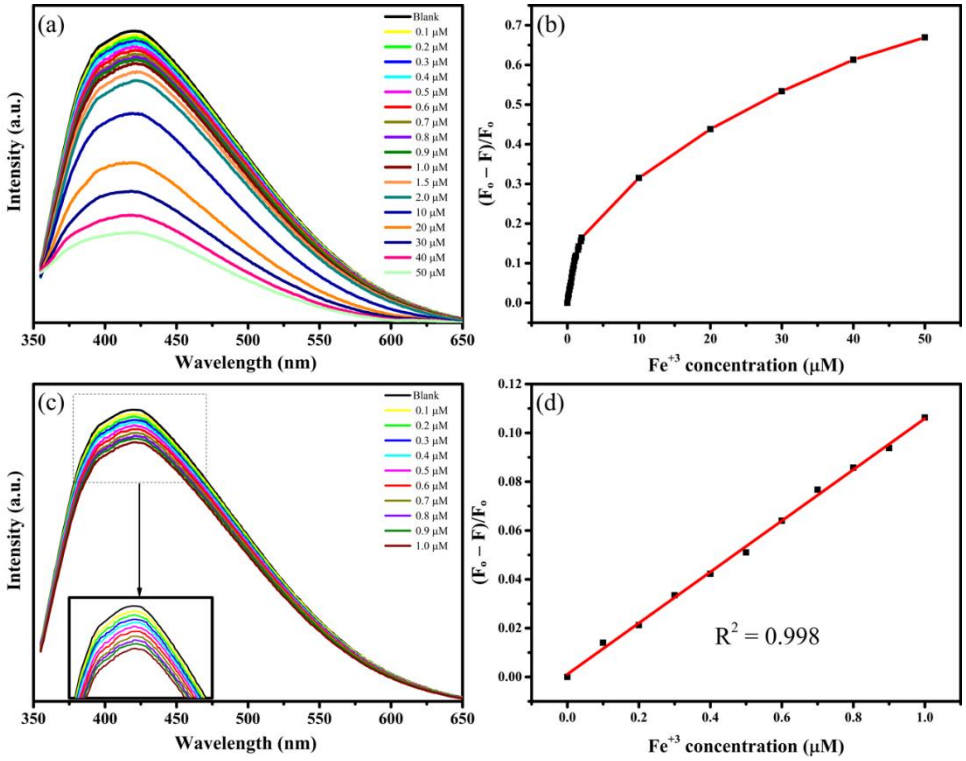

Fig. 14. (a) Photoluminescence spectra of C-500-GQDs (10 μg mL^{-1}) at different concentrations of Fe^{3+} ranging from 0 to 50 μM, at an excitation wavelength of 340 nm and (b) variation in the photoluminescence intensity as a function of Fe^{3+} concentration. (c) Photoluminescence spectra at low Fe^{3+} concentration from 0 to 1 μM (inset is the magnified image) and (d) corresponding linear regression plot between fluorescence intensity and Fe^{3+} concentration.

608 The calibration plot of quenching efficiency of Fe^{3+} was calculated by $(F_0 – F)/F_0$ and presented
609 in Fig. 14b. The quenching efficiency increases rapidly with increase in Fe^{3+} concentration at
610 low concentration range, while this increment slows down with increase in the concentration
611 range. Therefore, the quenching at lower range (0 to 1 µM) was further explored. Fig. 14c
612 demonstrates the photoluminescence spectra of C-500-GQDs at low Fe^{3+} concentration range
613 from 0 to 1 µM. The inset shows magnified image of peak intensities and a variation in intensity
614 with change in concentration can be clearly observed. In the low concentration range from 0 –
615 1 uM, a minute variation in concentration does not slow down the quenching efficiency and it
616 takes place almost linearly with Fe^{3+} concentration. Fig. 14d shows an excellent linear relation
617 between Fe^{3+} concentration at 0 to 1 µM range and the quenching efficiency. A linear
618 regression value (R^2) of 0.998 was acquired that indicates an excellent fit and precise sensing
619 of Fe^{3+} at even very low concentration. These findings suggest that C-500-GQDs can be
620 employed as a highly sensitive and selective probe for Fe^{3+} sensing.

621

622 Table 3. Comparison of the present study with previous promising studies for detection limit of Fe^{3+} by GQDs.

Sensing material	**Synthetic approach**	**Detection range (µM)**	**LOD (µM)**	**Ref.**
PEG-GQDs	Hydrothermal	0-60	5.77	[79]
GQDs	Electrochemical exfoliation	0-80	7.22	[48]
CQDs	Thermal reaction	0-20	0.041	[80]
N-CQDs	Hydrothermal	0-250	0.75	[81]
GQDs	Microwave treatment	0-50	2.5	[33]
N-GQDs	Hydrothermal	1-1945	0.09	[82]
GQDs	Chemical oxidation	0-60	0.45	[46]
GQDs	Hydrothermal	0-50	0.026	Present work

The limit of detection (LOD) was determined from equation: $\mathrm{LOD} = 3\frac{\sigma}{S}$, where σ is related to the intercept's standard deviation and S is associated with the slop of linear calibration plot. The LOD was determined to be 26 ± 0.4 nM. The LOD for Fe^{3+} determined in this work is lower than most of the previous studies summarised in Table 3. Moreover, the LOD identified in this work is considerably lower than the drinking water guideline limit of the World Health Organisation (WHO) for Fe^{3+} concentration (5.36 µM) [83]. Owing to their high quality, strong fluorescence, high solubility and extensive presence of specific surface functional groups, these GQDs demonstrate very low LOD for Fe^{3+} sensing. These findings imply that the present sensor is capable to detect trace amounts of Fe^{3+}. Hence, we strongly believe the C-500-GQDs possess promising potential for Fe^{3+} detection in real-world applications.

4. Conclusions

The role of precursor microstructure in the synthesis of GQDs was systematically investigated. The use of a partially carbonised precursor resulted in the synthesis of carbon nanodots and nanosheets, while sp^2 dominance and aromatic structure of the carbon precursor were found responsible for the development of high quality GQDs. The average size of GQDs prepared by hydrothermal treatment of sp^2 dominant carbon precursor was 11.6 ± 1.8 nm, with a thickness of 1-3 nm. The introduction of a novel and straightforward purification approach played a key role in achieving high purity GQDs. As-prepared GQDs exhibit fascinating optical properties with a moderate quantum yield of up to 17.5 %. Owing to their intriguing optical properties, these GQDs were employed as a fluorescence probe for the detection of nanomolar Fe^{3+}. A sensor was designed to selectively detect Fe^{3+} with a high sensitivity down to 26 ± 0.4 nM. This simple yet efficient approach shows the advantages of low cost, sustainability and

possibility of scale-up for synthesising high quality GQDs with high sensing capabilities. The present study highlights the significance of controlling precursor microstructure of low-value biomass resources to develop high-value nanomaterials for real-world applications.

Acknowledgements

This research is supported by the Faculty of Science, Agriculture & Engineering (SAgE), School of Engineering, and International Fund Partnership Newcastle University, United Kingdom (OSR/0530/SD16/ABBA). Authors appreciatively acknowledge the XPS data collection from the EPSRC National Facility for XPS (HarwellXPS), operated by Cardiff University and UCL, under contract no. PR16195. Authors thankfully acknowledge the valuable discussions with Prof. K Mark Thomas.

Data Availability

The data that supports the findings of this study are available from the corresponding author upon reasonable request.

References

[1] Y. Yan, J. Gong, J. Chen, Z. Zeng, W. Huang, K. Pu, J. Liu, P. Chen, Recent advances on graphene quantum dots: from chemistry and physics to applications, Adv. Mater., 31 (2019) 1808283.

[2] A. Abbas, L.T. Mariana, A.N. Phan, Biomass-waste derived graphene quantum dots and their applications, Carbon, 140 (2018) 77-99.

[3] D. Ghosh, K. Sarkar, P. Devi, K.-H. Kim, P. Kumar, Current and future perspectives of carbon and graphene quantum dots: From synthesis to strategy for building optoelectronic and energy devices, Renew. Sust. Energ. Rev., 135 (2021) 110391.

[4] S. Zhu, Y. Song, J. Wang, H. Wan, Y. Zhang, Y. Ning, B. Yang, Photoluminescence mechanism in graphene quantum dots: quantum confinement effect and surface/edge state, Nano Today, 13 (2017) 10-14.

[5] L.A. Ponomarenko, F. Schedin, M.I. Katsnelson, R. Yang, E.W. Hill, K.S. Novoselov, A.K. Geim, Chaotic Dirac Billiard in Graphene Quantum Dots, Science, 320 (2008) 356-358.

[6] X. Wang, G. Sun, N. Li, P. Chen, Quantum dots derived from two-dimensional materials and their applications for catalysis and energy, Chem. Soc. Rev., 45 (2016) 2239-2262.

[7] Y. Yan, J. Chen, N. Li, J. Tian, K. Li, J. Jiang, J. Liu, Q. Tian, P. Chen, Systematic Bandgap Engineering of Graphene Quantum Dots and Applications for Photocatalytic Water Splitting and CO2 Reduction, ACS nano, 12 (2018) 3523-3532.

[8] T.A. Tabish, C.J. Scotton, D.C.J. Ferguson, L. Lin, A.v.d. Veen, S. Lowry, M. Ali, F. Jabeen, M. Ali, P.G. Winyard, S. Zhang, Biocompatibility and toxicity of graphene quantum dots for potential application in photodynamic therapy, Nanomedicine, 13 (2018) 1923-1937.

[9] T.A. Tabish, F.A. Memon, D.E. Gomez, D.W. Horsell, S. Zhang, A facile synthesis of porous graphene for efficient water and wastewater treatment, Sci. Rep., 8 (2018) 1-14.

[10] J. Yang, H. Miao, J. Jing, Y. Zhu, W. Choi, Photocatalytic activity enhancement of PDI supermolecular via π-π action and energy level adjusting with graphene quantum dots, Appl. Catal. B, 281 (2021) 119547.

[11] M.G. Ashritha, S.R. Rondiya, R.W. Cross, N.Y. Dzade, S.D. Dhole, K. Hareesh, D.V. Sunitha, Experimental and computational studies of sonochemical assisted anchoring of carbon quantum dots on reduced graphene oxide sheets towards the photocatalytic activity, Appl. Surf. Sci., 545 (2021) 148962.

693 [12] A. Ibarbia, L. Sánchez-Abella, L. Lezama, H.J. Grande, V. Ruiz, Graphene quantum dot-based
694 hydrogels for photocatalytic degradation of organic dyes, Appl. Surf. Sci., 527 (2020) 146937.
695 [13] B. Li, X. Yu, X. Yu, R. Du, L. Liu, Y. Zhang, Graphene quantum dots decorated ZnO-ZnFe2O4
696 nanocages and their visible light photocatalytic activity, Appl. Surf. Sci., 478 (2019) 991-997.
697 [14] R. Riaz, M. Ali, I.A. Sahito, A.A. Arbab, T. Maiyalagan, A.S. Anjum, M.J. Ko, S.H. Jeong,
698 Self-assembled nitrogen-doped graphene quantum dots (N-GQDs) over graphene sheets for
699 superb electro-photocatalytic activity, Appl. Surf. Sci., 480 (2019) 1035-1046.
700 [15] X. Li, M. Rui, J. Song, Z. Shen, H. Zeng, Carbon and graphene quantum dots for optoelectronic
701 and energy devices: a review, Adv. Funct. Mater., 25 (2015) 4929-4947.
702 [16] Y. Lin, Z. Jiang, Z. Ouyang, Y. Lei, Z. Ouyang, J. Hu, P. Du, Y. Wu, Effect of graphene
703 quantum dots addition on photoelectric performances of CdSSe, Materials Science and
704 Engineering: B, 264 (2021) 114923.
705 [17] H. Lu, W. Li, H. Dong, M. Wei, Graphene Quantum Dots for Optical Bioimaging, Small, 15
706 (2019).
707 [18] H. Wang, Q. Chen, S. Zhou, Carbon-based hybrid nanogels: A synergistic nanoplatform for
708 combined biosensing, bioimaging, and responsive drug delivery, Chem. Soc. Rev., 47 (2018)
709 4198-4232.
710 [19] S. Chung, R.A. Revia, M. Zhang, Graphene Quantum Dots and Their Applications in
711 Bioimaging, Biosensing, and Therapy, Adv. Mater., DOI 10.1002/adma.201904362(2019).
712 [20] T.A. Tabish, S. Zhang, P.G. Winyard, Developing the next generation of graphene-based
713 platforms for cancer therapeutics: The potential role of reactive oxygen species, Redox Biol.,
714 15 (2018) 34-40.
715 [21] T.A. Tabish, L. Lin, M. Ali, F. Jabeen, M. Ali, R. Iqbal, D.W. Horsell, P.G. Winyard, S. Zhang,
716 Investigating the bioavailability of graphene quantum dots in lung tissues via Fourier transform
717 infrared spectroscopy, Interface Focus, 8 (2018) 20170054.
718 [22] Z. Huang, T. Zhou, Y. Yuan, S. Natalie Kłodzińska, T. Zheng, C. Sternberg, H. Mørck Nielsen,
719 Y. Sun, F. Wan, Synthesis of carbon quantum dot-poly lactic-co-glycolic acid hybrid

720 nanoparticles for chemo-photothermal therapy against bacterial biofilms, J. Colloid Interface
721 Sci., 577 (2020) 66-74.
722 [23] H. Tetsuka, T. Matsui, Non-ionic Fluorosurfactant Improves Wettability of Nitrogen-
723 functionalized Graphene Quantum Dots for Integration with Optoelectronic Devices, Chem.
724 Lett., 47 (2018) 850-852.
725 [24] F. Yuan, T. Yuan, L. Sui, Z. Wang, Z. Xi, Y. Li, X. Li, L. Fan, A. Chen, M. Jin, Engineering
726 triangular carbon quantum dots with unprecedented narrow bandwidth emission for
727 multicolored LEDs, Nature communications, 9 (2018) 2249.
728 [25] D.H. Kim, T.W. Kim, Ultrahigh-luminosity white-light-emitting devices based on edge
729 functionalized graphene quantum dots, Nano Energy, DOI (2018).
730 [26] D. Pan, J. Zhang, Z. Li, M. Wu, Hydrothermal route for cutting graphene sheets into blue-
731 luminescent graphene quantum dots, Adv. Mater., 22 (2010) 734-738.
732 [27] J. Peng, W. Gao, B.K. Gupta, Z. Liu, R. Romero-Aburto, L. Ge, L. Song, L.B. Alemany, X.
733 Zhan, G. Gao, S.A. Vithayathil, B.A. Kaipparettu, A.A. Marti, T. Hayashi, J.-J. Zhu, P.M.
734 Ajayan, Graphene Quantum Dots Derived from Carbon Fibers, Nano Lett., 12 (2012) 844-849.
735 [28] R. Ye, C. Xiang, J. Lin, Z. Peng, K. Huang, Z. Yan, N.P. Cook, E.L.G. Samuel, C.-C. Hwang,
736 G. Ruan, G. Ceriotti, A.-R.O. Raji, A.A. Martí, J.M. Tour, Coal as an abundant source of
737 graphene quantum dots, Nature Communications, 4 (2013) 2943.
738 [29] A. Abbas, S. Abbas, A. Bhattarai, N.M. Latiff, N. Wai, A.N. Phan, T.M. Lim, Effect of
739 electrode porosity on the charge transfer in vanadium redox flow battery, J. Power Sources, 488
740 (2021) 229411.
741 [30] A. Abbas, X.E. Eng, N. Ee, F. Saleem, D. Wu, W. Chen, M. Handayani, T.A. Tabish, N. Wai,
742 T.M. Lim, Development of reduced graphene oxide from biowaste as an electrode material for
743 vanadium redox flow battery, J. Energy Storage, 41 (2021) 102848.
744 [31] A. Abbas, Y.M. Yi, F. Saleem, Z. Jin, A. Veksha, Q. Yan, G. Lisak, T.M. Lim, Multiwall
745 carbon nanotubes derived from plastic packaging waste as a high-performance electrode
746 material for supercapacitors, J International Journal of Energy Research, n/a (2021) 1-12.

747 [32] M.K. Kumawat, M. Thakur, R.B. Gurung, R. Srivastava, Graphene quantum dots from
748 mangifera indica: application in near-infrared bioimaging and intracellular nanothermometry,
749 ACS Sustain. Chem. Eng., 5 (2017) 1382-1391.
750 [33] A. Abbas, T.A. Tabish, S.J. Bull, T.M. Lim, A.N. Phan, High yield synthesis of graphene
751 quantum dots from biomass waste as a highly selective probe for Fe3+ sensing, Scientific
752 Reports, 10 (2020) 21262.
753 [34] P. Roy, A.P. Periasamy, C. Chuang, Y.-R. Liou, Y.-F. Chen, J. Joly, C.-T. Liang, H.-T. Chang,
754 Plant leaf-derived graphene quantum dots and applications for white LEDs, New J. Chem., 38
755 (2014) 4946-4951.
756 [35] Z. Ding, F. Li, J. Wen, X. Wang, R. Sun, Gram-scale synthesis of single-crystalline graphene
757 quantum dots derived from lignin biomass, Green Chem., 20 (2018) 1383-1390.
758 [36] S. Jing, Y. Zhao, R.-C. Sun, L. Zhong, X. Peng, Facile and high-yield synthesis of carbon
759 quantum dots from biomass-derived carbons at mild condition, ACS Sustain. Chem. Eng., 7
760 (2019) 7833-7843.
761 [37] S. Thambiraj, R. Shankaran, Green synthesis of highly fluorescent carbon quantum dots from
762 sugarcane bagasse pulp, Appl. Surf. Sci., 390 (2016) 435-443.
763 [38] P.K. Yadav, V.K. Singh, S. Chandra, D. Bano, V. Kumar, M. Talat, S.H. Hasan, Green
764 synthesis of fluorescent carbon quantum dots from azadirachta indica leaves and their
765 peroxidase-mimetic activity for the detection of H2O2 and ascorbic acid in common fresh
766 fruits, ACS Biomater. Sci. Eng., 5 (2018) 623-632.
767 [39] S.Y. Lim, W. Shen, Z. Gao, Carbon quantum dots and their applications, Chem. Soc. Rev., 44
768 (2015) 362-381.
769 [40] J. Liu, Y. Geng, D. Li, H. Yao, Z. Huo, Y. Li, K. Zhang, S. Zhu, H. Wei, W. Xu, J. Jiang, B.
770 Yang, Deep Red Emissive Carbonized Polymer Dots with Unprecedented Narrow Full Width
771 at Half Maximum, Adv. Mater., 32 (2020) 1906641.
772 [41] S. Liu, J. Tian, L. Wang, Y. Zhang, X. Qin, Y. Luo, A.M. Asiri, A.O. Al-Youbi, X. Sun,
773 Hydrothermal treatment of grass: a low-cost, green route to nitrogen-doped, carbon-rich,

photoluminescent polymer nanodots as an effective fluorescent sensing platform for label-free detection of Cu (II) ions, Adv. Mater., 24 (2012) 2037-2041.

[42] A. Suryawanshi, M. Biswal, D. Mhamane, R. Gokhale, S. Patil, D. Guin, S. Ogale, Large scale synthesis of graphene quantum dots (GQDs) from waste biomass and their use as an efficient and selective photoluminescence on–off–on probe for Ag+ ions, Nanoscale, 6 (2014) 11664-11670.

[43] R. Das, H. Sugimoto, M. Fujii, P.K. Giri, Quantitative Understanding of Charge Transfer Mediated Fe3+ Sensing and Fast Photoresponse by N-doped Graphene Quantum Dots Decorated on Plasmonic Au Nanoparticles, ACS Appl. Mater. Interfaces, DOI (2020).

[44] P. Lesani, G. Singh, C.M. Viray, Y. Ramaswamy, D.M. Zhu, P. Kingshott, Z. Lu, H. Zreiqat, Two-Photon Dual-Emissive Carbon Dot-Based Probe: Deep-Tissue Imaging and Ultrasensitive Sensing of Intracellular Ferric Ions, ACS Appl. Mater. Interfaces, 12 (2020) 18395-18406.

[45] R.B. Mounsey, P. Teismann, Chelators in the treatment of iron accumulation in Parkinson's disease, Int. J. Cell Biol., 2012 (2012).

[46] X. Zhu, Z. Zhang, Z. Xue, C. Huang, Y. Shan, C. Liu, X. Qin, W. Yang, X. Chen, T. Wang, Understanding the selective detection of Fe3+ based on graphene quantum dots as fluorescent probes: the K sp of a metal hydroxide-assisted mechanism, Anal. Chem., 89 (2017) 12054-12058.

[47] X. Sun, Y. Lei, Fluorescent carbon dots and their sensing applications, TrAC, Trends Anal. Chem., 89 (2017) 163-180.

[48] A. Ananthanarayanan, X. Wang, P. Routh, B. Sana, S. Lim, D.H. Kim, K.H. Lim, J. Li, P. Chen, Facile synthesis of graphene quantum dots from 3D graphene and their application for Fe3+ sensing, Adv. Funct. Mater., 24 (2014) 3021-3026.

[49] J. Yu, N. Paterson, J. Blamey, M. Millan, Cellulose, xylan and lignin interactions during pyrolysis of lignocellulosic biomass, Fuel, 191 (2017) 140-149.

[50] R. Bilbao, A. Millera, J. Arauzo, Thermal decomposition of lignocellulosic materials: influence of the chemical composition, Thermochim. Acta, 143 (1989) 149-159.

[51] Z. Sun, M. Zheng, H. Hu, H. Dong, Y. Liang, Y. Xiao, B. Lei, Y. Liu, From biomass wastes to vertically aligned graphene nanosheet arrays: A catalyst-free synthetic strategy towards high-quality graphene for electrochemical energy storage, Chem. Eng. J., 336 (2018) 550-561.

[52] S. Jung, Y. Myung, B.N. Kim, I.G. Kim, I.-K. You, T. Kim, Activated Biomass-derived Graphene-based Carbons for Supercapacitors with High Energy and Power Density, Sci. Rep., 8 (2018) 1915.

[53] H. Yang, R. Yan, H. Chen, D.H. Lee, C. Zheng, Characteristics of hemicellulose, cellulose and lignin pyrolysis, Fuel, 86 (2007) 1781-1788.

[54] Y.-C. Lin, J. Cho, G.A. Tompsett, P.R. Westmoreland, G.W. Huber, Kinetics and mechanism of cellulose pyrolysis, The Journal of Physical Chemistry C, 113 (2009) 20097-20107.

[55] M. Brebu, C. Vasile, Thermal degradation of lignin—a review, Cellulose Chemistry & Technology, 44 (2010) 353.

[56] M.M. Nassar, G. MacKay, Mechanism of thermal decomposition of lignin, Wood and Fiber Science, 16 (2007) 441-453.

[57] A. Gani, I. Naruse, Effect of cellulose and lignin content on pyrolysis and combustion characteristics for several types of biomass, Renewable Energy, 32 (2007) 649-661.

[58] A. Gupta, G. Chen, P. Joshi, S. Tadigadapa, P.C. Eklund, Raman scattering from high-frequency phonons in supported n-graphene layer films, Nano Lett., 6 (2006) 2667-2673.

[59] F. Tuinstra, J.L. Koenig, Raman spectrum of graphite, J. Chem. Phys., 53 (1970) 1126-1130.

[60] E. Bekyarova, M.E. Itkis, P. Ramesh, C. Berger, M. Sprinkle, W.A. de Heer, R.C. Haddon, Chemical modification of epitaxial graphene: spontaneous grafting of aryl groups, J. Am. Chem. Soc., 131 (2009) 1336-1337.

[61] J.R. Pels, F. Kapteijn, J.A. Moulijn, Q. Zhu, K.M. Thomas, Evolution of nitrogen functionalities in carbonaceous materials during pyrolysis, Carbon, 33 (1995) 1641-1653.

[62] Z. Wang, J. Yu, X. Zhang, N. Li, B. Liu, Y. Li, Y. Wang, W. Wang, Y. Li, L. Zhang, Large-scale and controllable synthesis of graphene quantum dots from rice husk biomass: a comprehensive utilization strategy, ACS applied materials & interfaces, 8 (2016) 1434-1439.

[63] C. Hu, Y. Liu, Y. Yang, J. Cui, Z. Huang, Y. Wang, L. Yang, H. Wang, Y. Xiao, J. Rong, One-step preparation of nitrogen-doped graphene quantum dots from oxidized debris of graphene oxide, J Mater. Chem. B, 1 (2013) 39-42.

[64] M. Acik, G. Lee, C. Mattevi, M. Chhowalla, K. Cho, Y. Chabal, Unusual infrared-absorption mechanism in thermally reduced graphene oxide, Nature materials, 9 (2010) 840-845.

[65] L. Tang, R. Ji, X. Cao, J. Lin, H. Jiang, X. Li, K.S. Teng, C.M. Luk, S. Zeng, J. Hao, Deep ultraviolet photoluminescence of water-soluble self-passivated graphene quantum dots, ACS nano, 6 (2012) 5102-5110.

[66] S. Kim, S.W. Hwang, M.-K. Kim, D.Y. Shin, D.H. Shin, C.O. Kim, S.B. Yang, J.H. Park, E. Hwang, S.-H. Choi, Anomalous behaviors of visible luminescence from graphene quantum dots: interplay between size and shape, ACS nano, 6 (2012) 8203-8208.

[67] S. Kim, D. Hee Shin, C. Oh Kim, S. Seok Kang, S. Sin Joo, S.-H. Choi, S. Won Hwang, C. Sone, Size-dependence of Raman scattering from graphene quantum dots: interplay between shape and thickness, Appl. Phys. Lett., 102 (2013) 053108.

[68] L. Li, G. Wu, G. Yang, J. Peng, J. Zhao, J.-J. Zhu, Focusing on luminescent graphene quantum dots: current status and future perspectives, Nanoscale, 5 (2013) 4015-4039.

[69] S.N. Baker, G.A. Baker, Luminescent carbon nanodots: emergent nanolights, Angew. Chem. Int. Ed., 49 (2010) 6726-6744.

[70] L.L. Li, J. Ji, R. Fei, C.Z. Wang, Q. Lu, J.R. Zhang, L.P. Jiang, J.J. Zhu, A facile microwave avenue to electrochemiluminescent two-color graphene quantum dots, Adv. Funct. Mater., 22 (2012) 2971-2979.

[71] Z. Luo, Y. Lu, L.A. Somers, A.C. Johnson, High yield preparation of macroscopic graphene oxide membranes, J. Am. Chem. Soc., 131 (2009) 898-899.

[72] J. Tauc, R. Grigorovici, A. Vancu, Optical properties and electronic structure of amorphous germanium, physica status solidi (b), 15 (1966) 627-637.

[73] Q. Li, S. Zhang, L. Dai, L.-s. Li, Nitrogen-doped colloidal graphene quantum dots and their size-dependent electrocatalytic activity for the oxygen reduction reaction, J. Am. Chem. Soc., 134 (2012) 18932-18935.

[74] X. Yan, X. Cui, L.-s. Li, Synthesis of large, stable colloidal graphene quantum dots with tunable size, J. Am. Chem. Soc., 132 (2010) 5944-5945.

[75] M.A. Sk, A. Ananthanarayanan, L. Huang, K.H. Lim, P. Chen, Revealing the tunable photoluminescence properties of graphene quantum dots, Journal of Materials Chemistry C, 2 (2014) 6954-6960.

[76] H. Tetsuka, R. Asahi, A. Nagoya, K. Okamoto, I. Tajima, R. Ohta, A. Okamoto, Optically tunable amino-functionalized graphene quantum dots, Adv. Mater., 24 (2012) 5333-5338.

[77] G.S. Kumar, R. Roy, D. Sen, U.K. Ghorai, R. Thapa, N. Mazumder, S. Saha, K.K. Chattopadhyay, Amino-functionalized graphene quantum dots: origin of tunable heterogeneous photoluminescence, Nanoscale, 6 (2014) 3384-3391.

[78] Z. Liu, Z. Mo, X. Niu, X. Yang, Y. Jiang, P. Zhao, N. Liu, R. Guo, Highly sensitive fluorescence sensor for mercury(II) based on boron- and nitrogen-co-doped graphene quantum dots, J. Colloid Interface Sci., 566 (2020) 357-368.

[79] Y. Lou, J. Ji, A. Qin, L. Liao, Z. Li, S. Chen, K. Zhang, J. Ou, Cane Molasses Graphene Quantum Dots Passivated by PEG Functionalization for Detection of Metal Ions, ACS Omega, 5 (2020) 6763-6772.

[80] B. Chen, F. Li, L. Zou, D. Chen, Intermolecular hydrogen bonding-mediated synthesis of high-quality photoluminescent carbon dots for label-free fluorometric detection of Fe3+ ions, J. Colloid Interface Sci., 534 (2019) 381-388.

[81] H. Qi, M. Teng, M. Liu, S. Liu, J. Li, H. Yu, C. Teng, Z. Huang, H. Liu, Q. Shao, A. Umar, T. Ding, Q. Gao, Z. Guo, Biomass-derived nitrogen-doped carbon quantum dots: highly selective fluorescent probe for detecting Fe3+ ions and tetracyclines, J. Colloid Interface Sci., 539 (2019) 332-341.

879 [82] J. Ju, W. Chen, Synthesis of highly fluorescent nitrogen-doped graphene quantum dots for
880 sensitive, label-free detection of Fe (III) in aqueous media, Biosens. Bioelectron., 58 (2014)
881 219-225.
882 [83] W.H. Organization, Guidelines for drinking-water quality, World Health Organization1993.
883